Koponen, Lari; Nieminen, Jaakko; Mutanen, Tuomas; Stenroos, Matti; Ilmoniemi, Risto

Coil optimisation for transcranial magnetic stimulation in realistic head geometry

Published in:
Brain Stimulation

DOI:
10.1016/j.brs.2017.04.001

Published: 01/01/2017

Document Version
Peer-reviewed accepted author manuscript, also known as Final accepted manuscript or Post-print

Coil optimisation for transcranial magnetic stimulation in realistic head geometry

Lari M. Koponen Jaakko O. Nieminen

Tuomas P. Mutanen Matti Stenroos Risto J. Ilmoniemi

April 5, 2017

Department of Neuroscience and Biomedical Engineering, Aalto University, P.O. Box 12200, FI-00076 AALTO, Espoo, Finland.

BioMag Laboratory, HUS Medical Imaging Center, University of Helsinki and Helsinki University Hospital, P.O. Box 340, FI-00029 HUS, Helsinki, Finland.

Abstract

Background: Transcranial magnetic stimulation (TMS) allows focal, non-invasive stimulation of the cortex. A TMS pulse is inherently weakly coupled to the cortex; thus, magnetic stimulation requires both high current and high voltage to reach sufficient intensity. These requirements limit, for example, the maximum repetition rate and the maximum number of consecutive pulses with the same coil due to the rise of its temperature.

Objective: To develop methods to optimise, design, and manufacture energy-efficient TMS coils in realistic head geometry with an arbitrary overall coil shape.

Methods: We derive a semi-analytical integration scheme for computing the magnetic field energy of an arbitrary surface current distribution, compute the electric field induced by this distribution with a boundary

element method, and optimise a TMS coil for focal stimulation. Additionally, we introduce a method for manufacturing such a coil by using Litz wire and a coil former machined from polyvinyl chloride.

Results: We designed, manufactured, and validated an optimised TMS coil and applied it to brain stimulation. Our simulations indicate that this coil requires less than half the power of a commercial figure-of-eight coil, with a 41 % reduction due to the optimised winding geometry and a partial contribution due to our thinner coil former and reduced conductor height. With the optimised coil, the resting motor threshold of abductor pollicis brevis was reached with the capacitor voltage below 600 V and peak current below 3000 A.

Conclusion: The described method allows designing practical TMS coils that have considerably higher efficiency than conventional figure-of-eight coils.

Keywords

transcranial magnetic stimulation, coil design, optimization, boundary element method, induced electric field

1 Introduction

Transcranial magnetic stimulation (TMS) is a non-invasive brain-stimulation method. In TMS, a brief, strong pulse of current generates a rapidly changing magnetic field (B-field) that induces an electric field (E-field). With a suitable coil geometry, such as the figure-of-eight shape [1], a focal E-field distribution in the brain is induced. This, along with neuronavigation [2], has made TMS increasingly popular for both basic brain research and clinical applications, *e.g.*, for the treatment of drug-resistant major depression [3, 4].

To be effective, a TMS pulse requires both high current and high voltage, typically of the order of several kiloamperes and kilovolts, respectively. This causes several problems: the high current heats the coil due to resistive losses and exerts considerable mechanical forces in the coil windings, reducing their lifespan and causing a loud coil click. These issues are more severe with repetitive TMS used for, *e.g.*, depression treatment.

In [5], we introduced an optimisation method for designing TMS coils in spherical geometry. We showed that typical figure-of-eight coils are inefficient; for an equivalent stimulus, their B-field has almost four times the energy of the optimal coil. This minimum-energy coil, however, would be impractical for TMS, as it would surround almost the entire head. In [6], Sánchez *et al.* designed planar, spherical and hemi-spherical coils assuming spherically symmetric head geometry and using unconstrained weighted minimisation of the norm of error in the E-field and the B-field energy. As their approach contained no optimisation constraints for the focality, the same desired E-field distribution resulted in a different realised E-field distribution and focality for different coil geometries. To overcome the limitations of both previous approaches, we expand our constrained coil-optimisation method for any given overall coil shape and extent, providing a compromise between enhanced energy efficiency and usability, and describe how to build the optimisation constraints in a realistic head geometry.

We describe how to design, build, and test minimum-energy TMS coils for stimulating the human brain. First, we generalise the coil optimisation method introduced in [5] from the spherically symmetric head model to realistic head geometry to estimate better the true E-field distribution [7] and to enable modelling an arbitrary overall coil shape and extent instead of limiting the windings to lie on a spherical surface. Then, we design a coil using our method and present means for manufacturing and validating such a coil. Finally, we present data from a manufactured optimal coil.

2 Material and methods

Our aim is to find a coil that produces a desirable E-field distribution with minimal B-field energy. The B-field energy is proportional to the coil inductance times the square of its current. For a fixed coil geometry, the required current is inversely proportional to the number of turns in the windings and the inductance is proportional to the square of the number of turns. Thus, the optimisation has to consider the coil windings as a whole: we want to optimise the extent of the coil and the relative density of the windings in different parts of the coil. This optimisation problem consists of a set of constraints and a cost function. The constraints define the desirable shape of the E-field distribution: its focality and the location and orientation of its maximum. The cost function is the B-field energy. The optimum can be expressed by

$$\arg\min_{\boldsymbol{x}\in X} f(\boldsymbol{x}) \equiv \{\boldsymbol{x} \mid \boldsymbol{x} \in X \wedge \forall \boldsymbol{y} \in X : f(\boldsymbol{x}) \leq f(\boldsymbol{y})\} \ , \tag{1}$$

where $\boldsymbol{x}$ is the optimal and $\boldsymbol{y}$ a possible coil, X the set of all coils that produce the desirable E-field distribution, and f the B-field energy. Thus, we need to be able to compute the E-field distribution and the B-field energy of an arbitrary coil.

In [5], we solved this optimisation problem in spherical head geometry. The key was first to find the optimal surface current distribution that describes the

optimal coil and then to discretise this distribution to obtain the coil windings, instead of direct optimisation of the windings. The latter would be a typical high-dimensional non-linear problem for which there is no robust solver; most numerical solvers would either get stuck in a local minimum far from the global optimum or not converge at all, whereas the optimisation problem for the surface current density has a convex cost function and a convex set of constraints. Since the optimisation problem for the surface current distribution is convex, meaning that its cost function has no local minima, it can be solved efficiently [8]. In this article, we will retain the convex nature of the optimisation problem but change the underlying models for the coil, B-field energy, and E-field computation.

In [5], we used exclusively spherical symmetry and spherical harmonic functions. For spherically symmetric geometry, surface current constrained to a single close-to-head spherical shell was proven optimal, and series solutions for the E-field and the corresponding B-field energy was computed for such a shell. The optimal coil preferred the most efficient lowest-degree spherical harmonics, which resulted in a large coil with the farthest windings spanning under the chin if used on a real head. In this article, we extend our constrained optimisation method to realistically shaped head models and an arbitrary but fixed overall shape, *i.e.*, a set of arbitrary current-carrying surfaces with desired shape and limited extent (Fig. 1).

We require that the current-carrying surfaces have a quasi-static current distribution (no charge accumulation); such a distribution is described by a scalar stream function [9]. When the surfaces are discretised with small triangles with constant surface current density $\boldsymbol{K}_j$ in each triangle j, the stream function must be piecewise linear; such functions are described by the tent-function basis, where each basis function corresponds to an interior vertex with unit current flowing around it in the surrounding triangles (Fig. 2). The current density in each triangle is obtained as a weighted sum of the currents around its three vertices: $\boldsymbol{K}_j = \sum_i \boldsymbol{K}_{i,j}$, where $\boldsymbol{K}_{i,j} = \hat{\boldsymbol{b}}_{i,j} I_i / h_{i,j}$ and $\hat{\boldsymbol{b}}_{i,j}$ is the direction of the edge of triangle j opposite to vertex i, I_i the current around vertex i, and

$h_{i,j}$ the height of the triangle measured from vertex i. Having selected the discretisation, we need an efficient method for computing the TMS-induced E-field and the B-field energy for these elementary current loops. The former can be obtained using reciprocity and a boundary element method (BEM) in a way similar to that in [7]. For the latter, we derive a semi-analytical integration scheme.

2.1 Induced electric field

The induced E-field can be computed using reciprocity [10]:

$$[\boldsymbol{q} \cdot \boldsymbol{E}](\boldsymbol{r}) = -\int_S dS' \left[\frac{d\boldsymbol{M}}{dt} \cdot \boldsymbol{B}\right](\boldsymbol{r}') \ , \tag{2}$$

where $\boldsymbol{r}$ is the location of a (test) source-current dipole $\boldsymbol{q}$ inside a conducting medium, $\boldsymbol{B}$ the B-field produced by this source, $\boldsymbol{M}$ the instantaneous magnetic moment density of the TMS coil, t time, S the coil surface, and $\boldsymbol{E}$ the resulting E-field at $\boldsymbol{r}$. For the realistic head geometry, the B-field due to the source current was computed with an isolated-source linear-collocation BEM solver [11].

The E-field due to the ith elementary current loop with current I_i around vertex i is computed as follows: For each surrounding triangle j the total magnetic moment is

$$\boldsymbol{m}_{i,j} = (I_i S_j \hat{\boldsymbol{n}}_j)/3 \ , \tag{3}$$

where S_j is the area of the triangle and $\hat{\boldsymbol{n}}_j$ its normal vector (see Appendix A for the derivation). Thus, the rate of change of the corresponding magnetic moment density is

$$\frac{d\boldsymbol{M}_{i,j}}{dt} = \frac{\hat{\boldsymbol{n}}_j}{3}\frac{dI_i}{dt} \ . \tag{4}$$

If one evaluates numerically the right-hand side of Eq. (2) separately for each of the N elementary current loops, *e.g.*, with the Gaussian quadrature rule, for

three orthogonal unit source-current dipoles at N' different positions within the medium to obtain the E-field distribution, one obtains a $3N' \times N$ lead-field matrix, $\mathcal{L}$, such that

$$\boldsymbol{e} = \mathcal{L}\frac{d\boldsymbol{I}}{dt} \ , \tag{5}$$

where $\boldsymbol{e} = [E_{1,x}\ E_{1,y}\ E_{1,z}\ \ldots\ E_{N',z}]^{\mathrm{T}}$ and $\boldsymbol{I} = [I_1\ \ldots\ I_N]^{\mathrm{T}}$.

2.2 Magnetic field energy

Because the magnetic susceptibility of biological tissues does not differ much from that of vacuum and the electromagnetic penetration depth at the TMS-waveform frequencies of several kHz is of the order of 10 metres, the head has negligible impact on the B-field and we can compute it in free space. The B-field energy for a surface current distribution is

$$U = \frac{1}{2}\int_S dS\ [\boldsymbol{K}\cdot\boldsymbol{A}](\boldsymbol{r}) \ , \tag{6}$$

where S is the coil surface, $\boldsymbol{K}$ the surface current density, and $\boldsymbol{A}$ the magnetic vector potential given by

$$\boldsymbol{A}(\boldsymbol{r}) = \frac{\mu_0}{4\pi}\int_S dS'\ \frac{\boldsymbol{K}(\boldsymbol{r}')}{|\boldsymbol{r}-\boldsymbol{r}'|} \ . \tag{7}$$

For our elementary current loops, $\boldsymbol{K}$ is constant in each triangle. Thus, in Eq. (6), we essentially need to integrate the double surface integral of $1/|\boldsymbol{r}-\boldsymbol{r}'|$ over each triangle–triangle pair:

$$c_{k,l} = \int_{\mathrm{triangle}_k} dS \int_{\mathrm{triangle}_l} dS'\ \frac{1}{|\boldsymbol{r}-\boldsymbol{r}'|} \ . \tag{8}$$

When $k = l$, the inner integral is weakly singular: the integrand goes to infinity in the region of integration, but the integral has a well-defined finite value. This prevents numerical evaluation of the integral. Fortunately, the $1/r$ integral

over an arbitrary triangle has a closed-form solution [12].[1] With this solution, we can evaluate the inner integral at any point. This results in a well-behaving continuous finite integrand for the outer integral, which can be readily evaluated numerically, *e.g.*, with the Gaussian quadrature rule.

With the described semi-analytical integration scheme, the B-field energy computation is reduced to a bookkeeping problem. First, compute the double surface integrals $c_{k,l}$ for all triangle–triangle pairs; then, compute surface current-weighted sums of these integrals for each elementary current-loop pair:

$$U_{i,j} = \frac{\mu_0}{8\pi} \sum_{k \in \mathcal{I}} \sum_{l \in \mathcal{J}} c_{k,l} \left(\boldsymbol{K}_k \cdot \boldsymbol{K}_l \right) \ , \tag{9}$$

where $\mathcal{I}$ and $\mathcal{J}$ are the neighbourhoods of the ith and jth vertex, respectively.

Having computed the energy $U_{i,i}$ for each elementary current loop and the energy $U_{i,j}$ for each elementary current-loop pair, one can express the B-field energy of an arbitrary coil in quadratic form as

$$U = \frac{1}{2} \boldsymbol{I}^{\mathrm{T}} \mathbf{M} \boldsymbol{I} \ , \tag{10}$$

where

$$\mathbf{M} = \begin{bmatrix} L_1 & M_{1,2} & \cdots & M_{1,N} \\ M_{2,1} & L_2 & \cdots & M_{2,N} \\ \vdots & \vdots & \ddots & \vdots \\ M_{N,1} & M_{N,2} & \cdots & L_N \end{bmatrix} \tag{11}$$

and the self- and mutual inductances for the elementary current loops are obtained from their unit-current B-field energies as $L_i = 2U_{i,i}$ and $M_{i,j} = U_{i,j} - (U_{i,i} + U_{j,j})$, respectively.

[1] We used a Matlab (MathWorks, www.mathworks.com) implementation of this solution, which had been previously implemented and validated for [13].

2.3 Convex optimisation and interior-point method

A convex optimisation problem is of the form

$$\min_{\boldsymbol{x}\in X} f_0(\boldsymbol{x}) \tag{12}$$

where

$$X = \{\boldsymbol{x} \mid (\forall i \in \{1,\ldots,m\})\,[f_i(\boldsymbol{x}) \leq 0]\} \tag{13}$$

and the cost function f_0 and the constraint functions $f_1,\ldots,f_m$ are convex, *i.e.*, they satisfy the inequality

$$f(\alpha\boldsymbol{x} + \beta\boldsymbol{y}) \leq \alpha f(\boldsymbol{x}) + \beta f(\boldsymbol{y}) \tag{14}$$

for all $\boldsymbol{x}$ and $\boldsymbol{y}$ with non-negative α and β such that $\alpha + \beta = 1$ [8]. Any linear function of the lead-field matrix of Eq. (5), *e.g.*, any single component, or the norm of the induced E-field at any point is a convex function.

The interior-point method [14] is an efficient algorithm for solving convex optimisation problems. It works by first finding any feasible solution by, *e.g.*, solving the unconstrained convex problem of finding the most feasible solution (in our case, the most focal coil) and then translating the original problem into unconstrained convex form by translating the constraints into a so-called barrier function, with infinite values for non-feasible points and near-constant value for the feasible points, added to the cost function. This unconstrained problem can then be solved with Newton's method.[2]

2.4 Formulation of the optimisation problem

There are several practical challenges that affect the TMS coil design. The three most important ones are the high voltage required to achieve brief, strong current pulses, significant mechanical forces on the coil windings, and resistive

[2]We used the interior-point-method implementation of Matlab.

heating of the coil by the high current. The voltage driving the coil current can be several kV, requiring good electrical insulation to guarantee safety. The mechanical forces trying to pull the coil apart can be very high; the total outward radial force of a tightly wound coil is on the order of 10 kN [15], and we computed that the two wings of a typical figure-of-eight coil push each other apart with a force on the order of 1 kN (see Section 2.6). The resistive losses cause every pulse to heat the coil windings by

$$\Delta T \approx \frac{I^2 \Delta t}{2\sigma c \rho \mathcal{A}^2} \ , \tag{15}$$

where I is the peak current, Δt the pulse duration, σ electrical conductivity, c specific heat capacity, ρ density, and $\mathcal{A}$ the cross-sectional area of the wire; for a typical TMS pulse,

$$\Delta T \approx \frac{20\,^\circ\mathrm{C}}{\left(\mathcal{A}/1\,\mathrm{mm}^2\right)^2} \tag{16}$$

as derived in Appendix B. To overcome these challenges requires a strong coil former with sufficient electrical insulation and thick wires, which effectively set the minimum distance from the scalp to the windings and the minimum wire thickness.

Optimisation constraints

We define the optimal TMS coil as the one that produces a stimulus functionally equivalent to that of a typical figure-of-eight coil whilst requiring least power. That is, we want to minimise the B-field energy of Eq. (10) whilst retaining similar E-field in the region of interest. We consider the two E-field distributions to be functionally equivalent if they have the same maximum E-field in the cortex (location and orientation included) and have an equal region in the cortex where the induced E-field magnitude is above $1/\sqrt{2} \approx 70\,\%$ of that value. A more detailed formulation of this optimisation problem is given in Table 1.

The interior-point method implementation of Matlab assumes a set of linear

Table 1: The TMS-coil optimisation problem. The focal point is the location of the maximum E-field, $\boldsymbol{E}_0$, in the cortex and the focal region is the region where the induced E-field magnitude is above $1/\sqrt{2} \approx 70\,\%$ of the value at the focal point.

minimise	$U(\boldsymbol{I}) = \boldsymbol{I}^{\mathrm{T}}\mathbf{M}\boldsymbol{I}/2$
	$\boldsymbol{E} = \boldsymbol{E}_0$ at the focal point
	$E \leq E_0$ everywhere
	$E \leq E_0/\sqrt{2}$ outside the focal region

constraints in matrix notation. Thus, we need to express the nonlinear E-field norm constraint using a set of linear equations. In a two-dimensional (2-d) system, a constraint for the norm of a vector means that the end point of the vector must lie within a circle with the maximum allowed norm as the radius. A set of linear constraints is obtained by approximating the circle with a convex polygon, as is shown in Fig. 3 (left). In 2-d, the process for approximating the constraint for norm is straightforward; with 16 linear constraints per point, we obtain an estimate with maximum relative error of 0.014.

In realistic head geometry, the E-field is three-dimensional (3-d) and the constraints for the norm can be approximated using convex polyhedra; however, this extra dimension in the E-field complicates the approximation process. One cannot simply use any regular polyhedron, as even when using an icosahedron as the estimate for the norm the maximum relative error is 0.19, and to match the relative error obtained in 2-d with the 16-gon (0.014) requires, with a quasi-regular subdivision mesh from the icosahedron, the second subdivision with 320 elements. With this approach, there would be more than one hundred thousand constraints, making the problem slow to solve. We can improve this by almost a factor of two. For polyhedra consisting of triangle elements, their duals offer similar accuracy with (almost) halved element count. With the dual of the second subdivision of an icosahedron, we obtained a maximum relative error of 0.012 with 162 elements (Fig. 3, right), which resulted typically in 80000 constraints for the optimisation problem.

Optimisation procedure

Given the method above, we can optimise a TMS coil, with a given overall shape and outer boundary (Fig. 1), for stimulating a desired target with given focality constraints. Defining the focality constraints in a realistic head geometry is not as straightforward as it is in the spherical geometry, where the induced E-field distribution is inherently symmetric (for an antisymmetric coil held tangential to the scalp). We defined the focality constraints by first computing the E-field distribution produced by a conventional figure-of-eight coil at the same coil position and then building the constraints from this distribution. As the conventional coil, we used Magstim 70mm Double Coil (The Magstim Co Ltd, www.magstim.com), which we will refer to as the standard coil, and for which we built a model based on [16].

Because the coil optimisation described in this article is performed assuming a fixed overall coil shape and size, the shape has to be selected a priori. In [5], we showed for the spherical head geometry that a suitable coil that closely follows the scalp can produce exactly the same TMS-induced E-field as any other coil, but with the least energy, suggesting that curved coils are more efficient than planar coils or more complicated 3-d coils. The human head, however, has relatively complicated geometry, making it difficult to design a single curved coil that could be used everywhere on the head.

We studied five different overall coil shapes: (1) planar; (2–4) uniformly curved surfaces with radii of curvature of 40, 30, and 20 cm; and (5) "hat-like", with 4-cm-radius flat central part and smoothly curved exterior part, with a 2-cm offset towards the head compared to the planar coil at 9.5 cm from the coil centre which levels off at 4 cm by 15 cm from the centre similarly to the shape shown in Fig. 1. All five surface forms had circular symmetry to allow rotating the coil so that arbitrary E-field orientations can be obtained without the complication of changing coil-to-scalp distance. We defined the overall coil shapes by their bottom surfaces and assumed 4-mm-tall wire profile to lie in the volume 2–6 mm away from this surface. These windings were modelled with a

single mesh in the middle of this region, *i.e.*, 4 mm from the bottom surface. In the optimisation, we required the coil to be antisymmetric, *i.e.*, to consist of two symmetrical windings with current flowing in opposite directions, and to be placed at the same position and orientation as the standard coil.

We optimised the coils for the stimulation of the (estimated) hand region in the left primary motor cortex for 10 adult subjects (7 males, 3 females). The head models were built with FreeSurfer [17] for the MNE pipeline [18] with 2562 vertices on each of the three model surfaces (inner and outer skull surfaces and scalp) and 20484 vertices for computing the E-field at the boundary between grey and white matter. One of the head models is shown in Fig. 4. The final coil design was produced by averaging the ten highly-similar individually-optimised planar surface current distributions.

The studied overall coil shapes were required to have the same tilt as the standard coil placed tangentially on the scalp above the target, and were placed as close to the head as possible. The average, local head curvature would suggest that all coils fit tightly against the scalp, as the radius of curvature of each coil is larger than this curvature. Fitting the curved coil designs to realistic scalps over the motor cortex led to scalp–coil-bottom distances of 0–1.8 mm, 0–2.7 mm, and, excluding one subject, 0–4.8 mm, for the curved designs with the radius of curvature of 40, 30, and 20 cm, respectively. For the excluded subject, the centre of the 20-cm-curvature surface was more than 10 mm from the scalp, rendering the 20-cm-curvature coil unusable for that subject. The planar and the "hat-like" designs had zero distance between the scalp and the centre of the coil-former bottom for all ten subjects. This shows that some of the heads are far from spherical; in the sagittal plane the local scalp shape is often almost planar (Fig. 4). To determine if a curved coil will fit a subject, the individual scalp geometry is required.

2.5 Coil construction

A typical figure-of-eight coil consists of two sets of adjacent circular loops with opposite current directions. Thus, the wire can be wound, *e.g.*, around bobbins. The optimised TMS coils designed in this study have, however, more complicated winding patterns as shown in Fig. 5.

A suitable coil former can be manufactured from a durable non-magnetic plastic such as polyvinyl chloride (PVC). In this work, the coil former was machined from 10-mm-thick (bottom part) and 5-mm-thick (top part) PVC sheets. The grooves for the wire were 8 mm deep, leaving a uniform 2-mm-thick layer of PVC at the bottom, which alone was computed to provide both sufficient voltage insulation and mechanical strength. An illustration of the bottom part of the coil former is shown in Fig. 6.

The coil was wound with two parallel strands of Litz wire (Rudolf Pack GmbH & Co. KG, www.pack-feindraehte.de), which consisted of 70 individual circular strands with a diameter of 0.2 mm, glued into the grooves. This resulted in a total copper cross-sectional area of 4.4 mm^2. The final windings were designed by discretising the averaged surface current distribution with 18 loops along the contour lines of its stream function. The resulting loops were connected in a spiral-like fashion similarly to that in [9]. The number of loops was selected so that the winding density in the centre of the coil would be maximized with the selected wire. Coincidentally, the total number of loops matched that of the standard coil. Finally, a neuronavigation tracking unit (Nexstim Plc, www.nexstim.com) was attached to the coil (Fig. 6).

2.6 Computation of the properties of coil windings

The discretisation of the surface current distribution into coil windings is expected to reduce the efficiency slightly. To estimate the efficiency of the optimised coil in an unbiased manner in a geometry not used in the optimisation, we simulated the optimised coil windings using a spherically symmetric head

model with an 85-mm radius for the head, assuming a 15-mm distance between the scalp and the cortex. These dimensions match those used by, *e.g.*, [19], and those of our TMS-coil characteriser [20], which allows direct comparison between the simulated and measured quantities.

Induced E-field and the energy of the B-field

The E-field due to the coil windings can be computed by translating them back to the previously used basis functions, now, with discrete values for the elementary current-loop amplitudes. The B-field is obtained by computing the inductance of the discretised windings with well-known inductance calculation formulas [21]. For the inductance computation of the discretised windings, we assumed a 2-mm-thick circular wire.

Efficiency of the optimised coil windings

Assuming an identical pulse waveform for two coils, the peak current is inversely proportional to the ratio between the E-field and the rate of change of the coil current in each coil, that is, to the gain of that coil. Thus, the relative energy of two coils producing identical stimuli is

$$\frac{U_2}{U_1} = \frac{L_2/L_1}{(g_2/g_1)^2} \ , \tag{17}$$

where L is the inductance and g the gain.

Internal forces on coil windings

The magnetic forces on the windings can be computed from the work–energy principle [15] using finite-difference approximation:

$$\Delta U = -\int d\boldsymbol{x} \cdot \boldsymbol{F}(\boldsymbol{x}) \approx -\boldsymbol{F} \cdot \Delta\boldsymbol{x} \ , \tag{18}$$

where ΔU is the change in the B-field energy due to a displacement in the windings, $\boldsymbol{F}$ the force, and $\Delta\boldsymbol{x}$ the (small) displacement of a part of the coil

windings (here, one half of an antisymmetric coil). The force can be obtained by using three orthogonal displacements.

2.7 Experimental verification

For the experimental verification, the constructed coil was connected to our custom-made TMS device, which allows controlling the pulse duration and waveform. We used this device because, unlike our commercial device, it allows using a custom-built coil. A more detailed description of the device is included in Appendix C.

We measured the TMS-induced E-field distribution of the manufactured coil using our TMS-coil characteriser [20]. The coil current was measured using a Rogowski current probe (PEM CWT 60B, www.pemuk.com). We also measured the coil inductance using a test circuit consisting of the coil, a 100-Ω resistor, signal generator, and oscilloscope.

To verify the expected functionality of the designed coil in practice, we performed a TMS–electromyography (EMG) experiment with one right-handed adult male subject. The experiment was accepted by the Coordinating Ethics Committee of the Hospital District of Helsinki and Uusimaa and followed the Declaration of Helsinki. Before the experiment, the subject gave a written consent. We used a monophasic pulse with 60-µs rise time. To ensure consistent stimulation of the desired cortical region, we used the Nexstim NBS neuronavigation system. For neuronavigation, the subject had undergone magnetic resonance imaging with a 1-mm MPRAGE sequence. For measuring EMG, we used the Nexstim eXimia system.

Using the navigated instrument, we found the representation area of the right abductor pollicis brevis in the left primary motor cortex and measured the corresponding resting motor threshold (RMT). The RMT was defined as the lowest stimulus intensity producing a motor-evoked potential (MEP) with at least 50-µV peak-to-peak amplitude in at least 10 out of 20 trials [22]. We used a randomised interstimulus interval between 2 and 3 seconds.

During the experiment, the subject sat relaxed and wore hearing protection. For comparison, we also performed the same measurement using Nexstim eXimia Navigated Brain Stimulation System with a traditional figure-of-eight coil (Focal Monopulse, outer loop diameter 70 mm) and monophasic pulse with 70-µs rise time. The pulse waveforms for both devices are shown in Fig. C.2 in Appendix C. In addition to this, we determined the rate of change in the coil-former-bottom temperature at 150-% RMT for both systems. In this measurement, we gave pulses every 2 seconds whilst simultaneously measuring the temperature with a thermal camera (Flir i3, www.flir.eu).

3 Results

In this section, we present the optimisation results for different overall coil shapes, justify selecting the planar coil shape, and describe the results of experimental characterisation and validation of the optimised coil.

3.1 Coil optimisation

The optimised planar surface current distribution required 41.5 ± 0.8 % (mean $\pm$ standard deviation over ten subjects) of the energy of the standard coil (Magstim 70mm Double Coil) to produce an equally focal and strong stimulus. For mildly curved surfaces, the energy requirement was decreased to 36 ± 2 % and 35 ± 4 % for the radius of curvature of 40 cm and 30 cm, respectively. The worst-case scenario for these two, however, did not improve proportionally and required 41.2 % and 42.6 % of the standard coil energy, respectively, being similar to that of the planar surface (42.8 %). The smaller difference in the worst-case scenario is due to the curved surfaces not fitting tightly for all subjects. The hat-like surface was best both on average and in the worst case requiring 34.7 ± 0.8 % and 35.8 % of the energy of the standard coil, respectively.

Based on these results, most of the gain is already obtained with an optimised planar design. Thus, we manufactured a planar coil. The resulting 30 cm by

Table 2: The efficiency of the optimised coil compared to that of the standard coil. For the data of the first three rows, the inductance was simulated and the gain was simulated in a spherically symmetric head model. The relative peak force and energy were computed assuming identical pulse waveforms.

	Inductance µH	Gain $\frac{\mathrm{V/m}}{\mathrm{MA/s}}$	Force (rel.)	Energy (rel.)
Standard	15.2	1.41	1	1
Optimised	8.9	1.57	0.63	0.47
Optimised (with a 2.5-mm shim)	8.9	1.39	0.79	0.59
Optimised (measured)	9.0	1.59		0.46

20 cm coil former is shown in Fig. 6. The resulting coil was compared to the standard coil in the spherical geometry, where both simulation and measurement show that the optimised coil requires less than half peak B-field energy (Table 2). The optimised coil has 1-mm-thinner casing and 3-mm-shallower windings than the standard coil. To estimate their contribution to the improved efficiency, we simulated the optimised coil with a 2.5-mm shim below its bottom. The shim reduced the gain by 11 %; with the shim, the optimised coil required 41 % less energy than the standard coil.

The measured E-field distribution of the optimised coil looks like that of a typical figure-of-eight coil; the focal region is 56 mm by 32 mm, which is similar to that of the standard coil or other similarly sized figure-of-eight coils [20, Fig. 11]. The field distribution in directions parallel and perpendicular to the peak E-field and the field-distribution map are given in Fig. 7. The field distribution far from the focal region in the direction perpendicular to the stimulation direction is smoother than that of a typical figure-of-eight coil.

3.2 EMG experiment

The RMT was found to correspond to a capacitor voltage of 570 V, equal to a peak current of 2990 A, and a maximum stored energy of 40 J. At this intensity, the peak induced E-field measured with our TMS-coil characteriser [20] was 100 V/m. With the Nexstim system, the RMT was 46 % of the maximum

stimulator output, corresponding to 92 V/m with the TMS-coil characteriser. The locations for the motor "hot-spots" were 2 mm apart, which is of the order of the coil localisation error of the optical tracking hardware used in the neuronavigation system [2].

Having determined the RMT, we measured the rate of change in the coil temperature at 150 % RMT (Fig. 8). Starting from ambient temperature of 26.5 °C, we managed to give 181 pulses with the Nexstim system before the system detected that the coil was overheated. At this point, the peak surface temperature was 39.3 °C. With the optimised coil, the peak surface temperature rose to 38.5 °C after 600 pulses, after which the experiment was stopped.

4 Discussion

We developed a TMS-coil optimisation method in a realistic head geometry with an arbitrary overall coil shape and extent. We also presented a method for manufacturing such an optimised coil for actual TMS use and demonstrated with technical and physiological measurements the validity of our methods.

Compared to a traditional figure-of-eight design, with two adjacent circular wings, optimisation can increase TMS-coil efficiency by a factor of two with relatively simple changes to the winding pattern even when the optimised coil is constrained to be planar. The most obvious difference between the optimised and the standard coil is that the extent of the windings in the optimised coil is much larger whilst there is almost identical winding density in the centre of the coils. Because of this, the optimised coil has much lower inductance while retaining a similar coil–cortex coupling. Another smaller difference, not directly related to optimisation, is that the optimised coil has thinner coil-former bottom and thinner windings, which reduces the average distance from the windings to the scalp, which in turn increases the coupling to the cortex. Because of this, we obtained a 13-% increase in the coil–cortex coupling. The figure-of-eight coils used in this study for comparison (Magstim 70mm Double Coil and

Nexstim Focal Monopulse) are not necessarily the most efficient commercial coils available; however, they both represent the widely adapted figure-of-eight coil design. Our coil was optimised for focal stimulation of the primary motor cortex. The optimal coil for some specific target in another brain area might have different geometry. For example, the higher curvature of the skull above the mid-dorsolateral frontal cortex might allow a more curved coil design.

The optimised coil had far slower heat-up than the conventional coil, which is at least partially explained by the increased efficiency. There are, however, several other factors not related to the coil geometry, such as our shorter pulse duration (Fig. C.2) and the use of Litz wire,[3] which contribute towards slower heat-up. Greater gains can be achieved with curved overall coil shapes; such designs cannot, however, as easily substitute existing TMS coils because of the differences in scalp curvature between subjects and stimulation sites.

4.1 E-field model

We used three-layer boundary-element head models and a BEM solver for computing the TMS-induced E-field. One can, however, substitute these with any other model or method that can compute the external B-field due to a unit source-current dipole in the brain, *e.g.*, those used for solving the magnetoencephalography forward problem. If one chooses to use a spherically symmetric head model, the focality constraints can be defined in 2-d [5] and the optimisation will be two orders of magnitude faster. This can be useful if one plans, *e.g.*, to study the compromise between the size of the coil and its efficiency.

In this work, we considered focal stimulation of the primary motor cortex, observing that the individually-optimised coils were very similar in shape, and relative efficiency compared to the standard coil, when the coil surface did fit the subject (that is, when there was no gap between the scalp and the centre of the coil former). This lack of difference was somewhat expected based on [7], where the spherical model was considered adequate for estimating the E-field

[3]The Nexstim Focal Monopulse coil has solid copper windings.

at the motor cortex. Based on that study, we would expect little difference between the optimised coils resulting from a three-layer model or a four-layer model that includes the cerebrospinal fluid, but we would expect to see larger differences between the spherical and the three-layer models in more frontal regions or for optimisation of coils for deep TMS. Based on our observations on the importance of the coil having a perfect fit, we would discourage the use of a spherical model alone when designing non-planar coils, as it does not contain the necessary information of the scalp geometry even for the otherwise highly spherically-symmetric region above the motor cortex. When designing planar coils, a locally fitted spherical model might be sufficient in most cases. However, such a model would require anatomical information similar to that needed in our BEM approach (namely, the inner-skull surface and scalp). The difference between computation times for spherical and realistic geometries is not significant for coil optimisation—the field computation and the optimisation take only a few minutes on a desktop workstation for one coil location. Thus, the total computation time for all simulations in this paper was of the order of a few hours. In summary, making the local-spherical approximation is unnecessary, and may cause inaccurate results.

4.2 EMG experiment

Because our optimised coil is much larger than a conventional figure-of-eight coil, and because it does not have a handle for one-handed operation, it required a two-handed grip from the sides. With this grip and the neuronavigation, the coil was easy to hold steadily above the motor cortex. In the EMG experiment, the peak E-field corresponding to stimulation at RMT was 10 % higher with the optimised coil than with the Nexstim Focal Monopulse. This difference in peak E-field is likely due to the two systems having different pulse waveforms, with the Nexstim system having longer pulse duration (Fig. C.2), as these RMT measurement were made during the same day using identical randomised inter-stimulus interval of 2–3 s. At this short interstimulus interval, the responses of

consecutive pulses may interact with each other [23]; however, this interaction should be similar with both coils.

4.3 Iron core

Similarly to our previous work [5], we have only considered an air coil, that is, a coil without a magnetic core. An iron core can increase the energy efficiency of a TMS coil considerably [24]; however, this increase comes at a cost of increased bulkiness and weight due to the heavy core. In addition, the input–output curve of an iron-core coil at high stimulation intensities is non-linear due to the saturation of the core. In some applications, the benefit of further increase in efficiency may overcome the cost, and an iron core is reasonable. In those cases, the described optimisation method, or even to some extent an optimised air coil, could be used to even further increase the efficiency as an iron core can be interpreted to effectively suppress the B-field energy contribution from above the windings whilst the B-field below the windings is retained unchanged for an identical (minimum energy with given focality) stimulation of the brain.

4.4 Coil inductance

The optimised coil has, for the same number of turns, considerably lower inductance than a comparable standard coil, since its windings are distributed over a larger region (see Figs. 5 and 6). The lower inductance reduces the voltage required for a given current pulse. At the same time, the optimised coil couples better to the cortex, which reduces the current needed to induce a given E-field intensity. If one wishes to retain the TMS-pulse duration with a conventional TMS device, one must either adjust the capacitance in the TMS device or the number of turns in the coil windings to match the coil inductance to that of the previous coil. The latter change requires thinner wires, but as the required coil current is reduced proportionally, this does not contribute to a more rapid rise in the coil temperature. One should also note that the reduction in coil inductance is much less of an issue when using a stimulator with controllable

pulse duration such as the one in [25] or the one used in this study.

Because the optimised coil requires lower power for the stimulus itself, an optimised coil is relatively more sensitive to stray system parameters, such as the inductance in the power cord for the TMS coil. In our case, a temporary power cord visible in Fig. 6, a simple four-meter-long twisted pair, accounted for approximately 20 % of the total system inductance, decreasing the ratio between the coil gain and its inductance from 0.175 to 0.141 (V/m)/V. With an improved power cord of a commercial TMS coil, the extra inductance was reduced to an almost negligible level.

4.5 Inductance matrix

The inductance matrix (Eq. 11) is positive definite and full rank for non-closed surfaces. For closed surfaces, such as a spherical surface surrounding the head, the matrix has one zero eigenvalue with eigenvector $[1\ 1\ \ldots\ 1]^{\mathrm{T}}$, which corresponds to having zero current density in all triangles. This zero eigenvalue renders the optimisation numerically unstable for closed coil surfaces. The stability is regained by constraining the current at any single vertex to zero with no loss of generality.

Computing the inductance matrix of Eq. (11) is relatively laborious; however, the computation can be made significantly faster by noticing that the problem is almost embarrassingly parallel: each triangle–triangle pair can be computed independently of each other and each elementary current-loop pair can be computed independently of each other. Our current implementation can compute the inductance matrix for one high-resolution overall coil shape in under 10 minutes on a desktop workstation computer.

5 Conclusion

The developed coil optimisation method can be used to design more efficient TMS coils of any desired overall shape and size. As the optimised coils require

lower power, they might enable the use of smaller, and thus cheaper, power electronics in the future. Energy-efficient coils also make it easier to produce briefer TMS pulses, which would otherwise require higher voltage and peak power for equivalent stimulation intensity [26, 27], and thus more complicated power electronics [28]. Briefer pulses would cause less coil heating and offer less perceptible coil click [28].

Acknowledgements

The three-layer head models were made by Lauri Parkkonen. The coil former parts were manufactured by Enna Rane (Aalto University Design Factory). High-performance computing cluster resources of Aalto Science-IT project were used to develop and optimise the inductance-matrix-computation algorithm. The improved power cord and its connector were donated by Nexstim Plc.

This work was supported by the Finnish Cultural Foundation and the Academy of Finland (Decisions No. 255347, 265680, and 294625).

A Magnetic moment of a triangle

We derive the magnetic moment, $\boldsymbol{m}$, of a triangle element with a constant surface current density $\boldsymbol{K}$ parallel with the base of the triangle. First, move the top of the triangle to the origin, rotate it into the xy plane, and orient its base along the y axis. Then,

$$\boldsymbol{m} = \frac{1}{2}\int_{\text{triangle}} dS\ (\boldsymbol{r}\times\boldsymbol{K}) \tag{19}$$

$$= \frac{1}{2}\int_0^h dx \int_{b_1 x/h}^{b_2 x/h} dy\ (xK\hat{\boldsymbol{z}}) \tag{20}$$

$$= \frac{1}{2}\int_0^h dx\ \frac{Kb\hat{\boldsymbol{z}}}{h}x^2 \tag{21}$$

$$= \frac{1}{2}\frac{Kb\hat{\boldsymbol{z}}}{h}\frac{h^3}{3} = \frac{1}{3}(Kh)\frac{bh\hat{\boldsymbol{z}}}{2}\ , \tag{22}$$

where the parameters are defined in Fig. A.1. Finally, substituting $I = Kh$ and $S\hat{\boldsymbol{n}} = bh\hat{\boldsymbol{z}}/2$, where S is the area of the triangle and $\hat{\boldsymbol{n}}$ its normal vector, we identify the magnetic moment of the triangle

$$\boldsymbol{m} = \frac{S\hat{\boldsymbol{n}}}{3} I \ . \tag{23}$$

B Resistive heating of a coil

We derive a formula for the resistive heating of TMS-coil windings. Examine a piece of wire with length l, cross-sectional area $\mathcal{A}$, density ρ, conductivity σ, and specific heat capacity c. Omitting the skin and proximity effects, the piece has resistance

$$R = \frac{l}{\sigma \mathcal{A}} \tag{24}$$

and heat capacity

$$C = c\rho l \mathcal{A} \ . \tag{25}$$

According to Joule heating and Ohm's law, the power dissipated in a resistor is

$$P(t) = R\left[I(t)\right]^2 \ . \tag{26}$$

The total energy to heat the wire is obtained as the integral of this power over time; for a sinusoidal TMS pulse,

$$U = \int dt \ P(t) = \frac{RI_0^2}{2} \Delta t \ , \tag{27}$$

where I_0 is the peak current and Δt is the pulse duration. Thus, the change in the coil temperature is

$$\Delta T = \frac{U}{C} = \frac{I_0^2 \Delta t}{2\sigma c \rho \mathcal{A}^2} \ , \tag{28}$$

For copper wire and a typical TMS pulse lasting 330 µs with a peak current of 5000 A,

$$\Delta T \approx \frac{20\,^\circ\mathrm{C}}{\left(\mathcal{A}/1\,\mathrm{mm}^2\right)^2} \ . \tag{29}$$

C TMS device with controllable pulse waveform

We used a custom-made TMS device with circuit design similar to [29, 30, 31], which allows controlling the pulse duration and waveform. The circuit topology is shown in Fig. C.1; the capacitor is Electronicon E50.R34-105NT0 (1020 µF, www.electronicon.com) and the insulated-gate bipolar transistors are ABB 5SNA 1500E330305 (www.abb.com).

Figure C.2 shows the pulse waveforms of our device and the Magstim and Nexstim systems mentioned in the main text. The different pulse waveforms require different maximum E-field magnitudes to produce equal stimulation; however, this has no effect on the optimisation results shown in Table 2, as those results were computed assuming that all coils had the same waveform.

References

[1] Ueno S, Tashiro T, Harada K. Localized stimulation of neural tissues in the brain by means of a paired configuration of time-varying magnetic fields. J Appl Phys 1988;64:5862–4.

[2] Ruohonen J, Karhu J. Navigated transcranial magnetic stimulation. Clin Neurophysiol 2010;40:7–17.

[3] Pascual-Leone A, Rubio B, Pallardó F, Catalá MD. Rapid-rate transcranial magnetic stimulation of left dorsolateral prefrontal cortex in drug-resistant depression. Lancet 1996;348:233–7.

[4] George MS, Lisanby SH, Avery D, McDonald WM, Durkalski V, Pavlicova M, et al. Daily left prefrontal transcranial magnetic stimulation therapy for major depressive disorder: a sham-controlled randomized trial. Arch Gen Psychiatry 2010;67:507–16.

[5] Koponen LM, Nieminen JO, Ilmoniemi RJ. Minimum-energy coils for transcranial magnetic stimulation: application to focal stimulation. Brain Stimul 2015;8:124–34.

[6] Sánchez CC, Rodriguez JMG, Olozábal ÁQ, Blanco-Navarro D. Novel TMS coils designed using an inverse boundary element method. Phys Med Biol 2017;62:73–90.

[7] Nummenmaa A, Stenroos M, Ilmoniemi RJ, Okada YC, Hämäläinen MS, Raij T. Comparison of spherical and realistically shaped boundary element head models for transcranial magnetic stimulation navigation. Clin Neurophysiol 2013;124:1995–2007.

[8] Boyd S, Vandenberghe L. Interior-point methods. In: Convex Optimization. 7th printing with corrections. Cambridge University Press. 2004, pp. 561–620.

[9] Peeren GN. Stream function approach for determining optimal surface currents. J Comput Phys 2003;191:305–21.

[10] Heller L, van Hulsteyn DB. Brain stimulation using electromagnetic sources: theoretical aspects. Biophys J 1992;63:129–38.

[11] Stenroos M, Sarvas J. Bioelectromagnetic forward problem: isolated source approach revis(it)ed. Phys Med Biol 2012;57:3517–35.

[12] Graglia RD. On the numerical integration of the linear shape functions times the 3-d Green's function or its gradient on a plane triangle. IEEE Trans Antennas Propag 1993;41:1448–55.

[13] Stenroos M, Haueisen J. Boundary element computations in the forward and inverse problems of electrocardiography: comparison of collocation and Galerkin weightings. IEEE Trans Biomed Eng 2008;55:2124–33.

[14] Karmarkar N. A new polynomial-time algorithm for linear programming. Combinatorica 1984;4:373–95.

[15] Ilmoniemi RJ, Ruohonen J, Karhu J. Transcranial magnetic stimulation—a new tool for functional imaging of the brain. Crit Rev Biomed Eng 1999;27:241–84.

[16] Thielscher A, Kammer T. Linking physics with physiology in TMS: a sphere field model to determine the cortical stimulation site in TMS. NeuroImage 2002;17:1117–30.

[17] Fischl B. FreeSurfer. NeuroImage 2012;62:774–81.

[18] Gramfort A, Luessi M, Larson E, Engemann DA, Strohmeier D, Brodbeck C, et al. MNE software for processing MEG and EEG data. NeuroImage 2014;86:446–60.

[19] Deng Z-D, Lisanby SH, Peterchev AV. Electric field depth–focality tradeoff in transcranial magnetic stimulation: simulation comparison of 50 coil designs. Brain Stimul 2013;6:1–13.

[20] Nieminen JO, Koponen LM, Ilmoniemi RJ. Experimental characterization of the electric field distribution induced by TMS devices. Brain Stimul 2015;8:582–9.

[21] Grover FW. Inductance calculations, working formulas and tables. New York: Van Nostrand Reinhold; 1946.

[22] Rossini PM, Burke D, Chen R, Cohen LG, Daskalakis Z, Di Iorio R, et al. Non-invasive electrical and magnetic stimulation of the brain, spinal cord, roots and peripheral nerves: Basic principles and procedures for routine clinical and research application. An updated report from an IFCN Committee. Clin Neurophysiol, 2015;126:1071–107.

[23] Möller C, Arai N, Lücke J, Ziemann U. Hysteresis effects on the input–output curve of motor evoked potentials. Clin Neurophysiol, 2009;120:1003–8.

[24] Epstein CM, Davey KR. Iron-core coils for transcranial magnetic stimulation. J Clin Neurophysiol 2002;19:376e81.

[25] Peterchev AV, Jalinous R, Lisanby SH. A transcranial magnetic stimulator inducing near-rectangular pulses with controllable pulse width (cTMS). IEEE Trans Biomed Eng 2008;55:257–66.

[26] Barker AT, Garnham CW, Freeston IL. Magnetic nerve stimulation: the effect of waveform on efficiency, determination of neural membrane time constants and the measurement of stimulator output. Electroencephalogr Clin Neurophysiol 1991;S43:227–37.

[27] Peterchev AV, Goetz SM, Westin GG, Luber B, Lisanby SH. Pulse width dependence of motor threshold and input–output curve characterized with controllable pulse parameter transcranial magnetic stimulation. Clin Neurophysiol 2013;124:1364–72.

[28] Peterchev AV, Murphy DL, Goetz SM. Quiet transcranial magnetic stimulation: status and future directions. In: 2015 37th Annual International Conference of the IEEE Engineering in Medicine and Biology Society (EMBC). IEEE; 2015, pp. 226–9.

[29] Perreault DJ, Mogren S. Magnetic stimulator power and control circuit. U.S. Patent 6,551,233, issued April 22, 2003.

[30] Gattinger N, Moeßnang G, Gleich B. flexTMS—a novel repetitive transcranial magnetic stimulation device with freely programmable stimulus currents. IEEE Trans Biomed Eng 2012;59:1962–70.

[31] Peterchev AV, D'Ostilio K, Rothwell JC, Murphy DL. Controllable pulse parameter transcranial magnetic stimulator with enhanced circuit topology and pulse shaping. J Neural Eng 2014;11:056023.

Figure 1: An example of an overall coil shape with one surface with a flat central part and a curved exterior part.

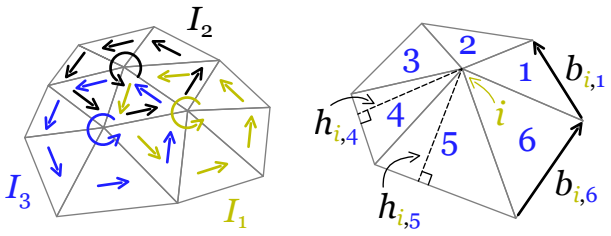

Figure 2: Left: The discretisation of the surface current in a triangular mesh. Each interior vertex i has a current I_i revolving around it in the surrounding triangles, with each triangle having a constant surface current density $\boldsymbol{K}_j = \sum_i \boldsymbol{K}_{i,j}$, where j denotes a triangular element and the summation is over its vertices. Right: An illustration of the indices and geometrical properties of a triangular mesh.

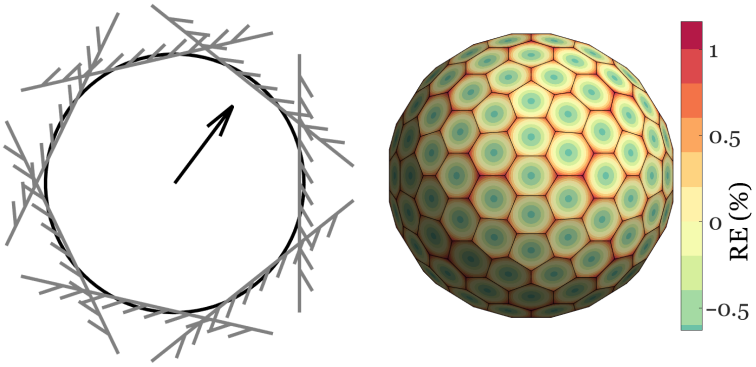

Figure 3: Left: A heptagon approximation for norm in 2-d. An inequality constraint for the norm means that the end point of the vector must reside inside the circle, which, in turn, can be approximated with an intersection of several half-planes each defined by one linear inequality. In 3-d, each linear inequality defines a half-space. Right: An illustration of the dual of the second subdivision of an icosahedron (with 162 elements) and the resulting distribution of relative error (RE) in the constraint for the norm.

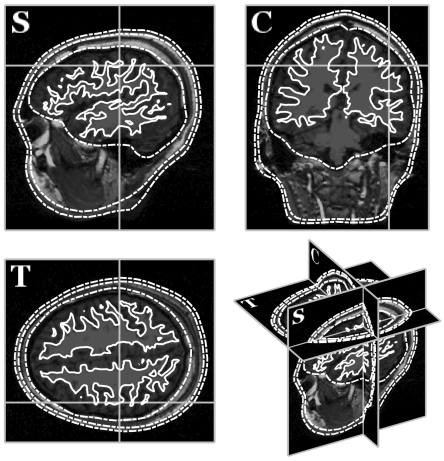

Figure 4: A three-layer head model overlaid on the corresponding MR image. The three meshes are drawn with dashed lines and the boundary between grey and white matter with solid line. The grey crosshairs indicates the location of the estimated hand region and the letters **T**, **C**, and **S** indicate the orientations of the different cross sections.

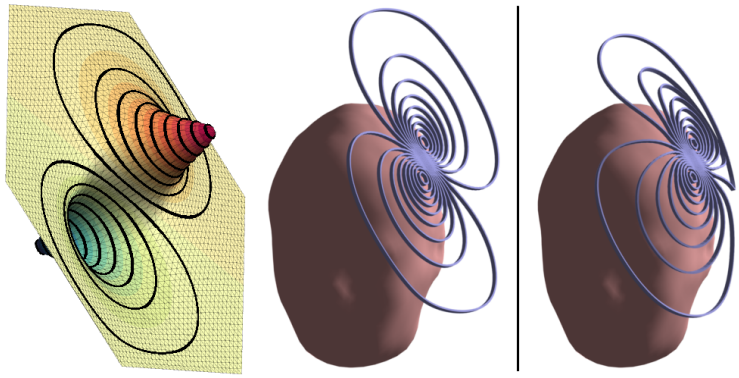

Figure 5: The coil windings follow the contour lines of the optimised elementary current-loop-amplitude distribution. The axis normal to the hexagon indicates the amount of current revolving around a vertex in its surrounding triangles; see Fig. 2. Left–middle: the optimised elementary current-loop-amplitude distribution and the resulting planar coil; right: the optimised "hat-like" coil.

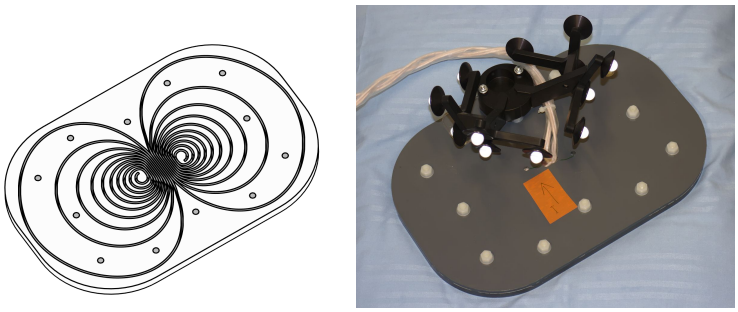

Figure 6: Left: An illustration of the bottom part of the coil former of the optimised coil. Right: The optimised TMS coil with a tracking unit.

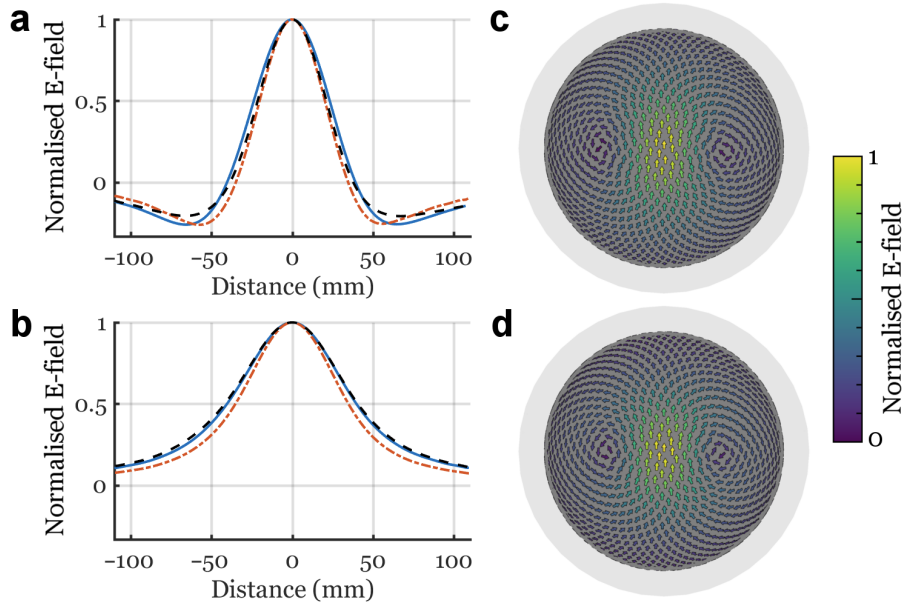

Figure 7: The TMS-induced E-field distribution as measured by our TMS-coil characteriser on a spherical surface with a radius of 70 mm when the coil bottom was at 85 mm from the origin of the spherical head model. Distribution in the direction perpendicular (**a**) and parallel (**b**) to the peak E-field for Magstim 70mm Double Coil (−), Nexstim Focal Monopulse (−·), and the optimised coil (−−). E-field distributions for the optimised coil (**c**) and the Nexstim coil (**d**). The data of the commercial coils have been previously presented in [20].

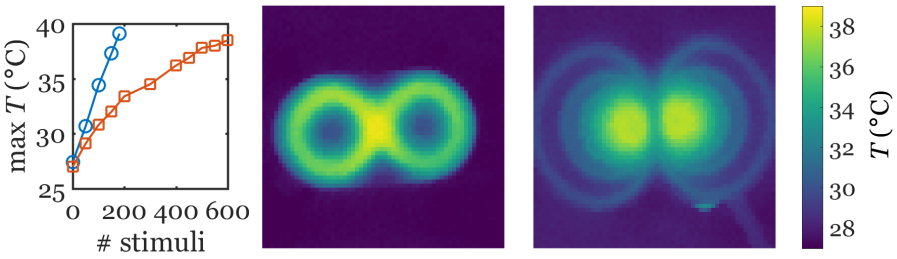

Figure 8: Left: The peak temperature, T, for the coil bottom for the Nexstim Focal Monopulse (○) and the optimised coil (□). Middle: The temperature of the Nexstim coil bottom after 181 pulses. Right: The temperature of the optimised coil bottom after 600 pulses.

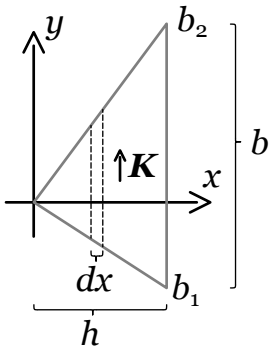

Figure A.1: A triangle in the xy plane with its base oriented parallel to the y axis.

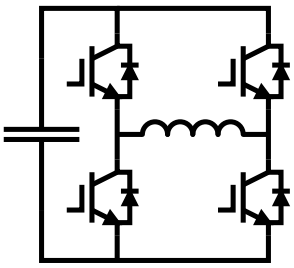

Figure C.1: A single-phase full-bridge inverter topology for TMS.

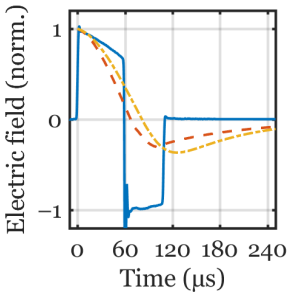

Figure C.2: The pulse waveforms of our device (solid blue line), the Nexstim eXimia Navigated Brain Stimulation System with their Focal Monopulse coil (red dashed line), and Magstim 200^2 with their 70mm Double Coil (yellow dash-dotted line). The waveforms of the commercial coils are from [20], and were sampled at 200 kHz; the data of our device were sampled at 80 MHz and low-pass filtered at 1 MHz.